Methanol Steam Reformer on a Silicon Wafer

Hyung Gyu Park, Jonathan A. Malen, W. Thomas Piggott, III, Jeffrey D. Morse, Ralph Greif, Costas P. Grigoropoulos, *ASME, Fellow*, Mark A. Havstad, and Ravi Upadhye

***Abstract*—A study of the reforming rates, heat transfer and flow through a methanol reforming catalytic microreactor fabricated on a silicon wafer are presented. Packed bed microchannel reactors were fabricated using silicon DRIE, followed by wafer bonding. The reactor bed was subsequently filled with catalyst particles. Thermal control is achieved through on-chip resistive heaters, whereby methanol steam reforming reactions were studied over a temperature range from 180–300 °C. Three simulations of varying complexity, including three-dimensional (3-D), quasi-3-D, and 1-D models, were developed. Comparison of the models with experimental results shows good agreement over a range of operating conditions. We found that Amphlett's kinetics for methanol reforming provided accurate results, and that for our operating conditions the reforming reaction could be modeled without mass transport considerations. The 1-D model provided a rapid analytical tool to assess the performance of the microreactor. Use of such computationally efficient design tools provides an effective means to analyze the performance of microreactor designs prior to fabrication and test. Hence, reformer geometry, catalyst loading, and operating parameters can be optimized to afford the desired hydrogen output and conversion. Concepts for insulating the reactor while maintaining small overall size are further analyzed. [1362]**

***Index Terms*—Heat transfer, methanol reforming, microreactor.**

NOMENCLATURE

A	Surface area (m^2).
A_c	Channel cross sectional area (m^2).
a_p	Surface area per unit volume of catalyst pellet $(\mathrm{m}^2/\mathrm{m}^3)$.
C_{Amp}	Empirically determined reaction modification factor.
c_i	Concentration of species i $(\mathrm{mol}/\mathrm{m}^3)$.
C_1, C_2	Convective heat transfer coefficients.
c_p	Heat capacity (J/kg·K).
D_{12}	Binary diffusion coefficient $(\mathrm{m}^2/\mathrm{s})$.
D_{1m}	Mixture diffusion coefficient $(\mathrm{m}^2/\mathrm{s})$.
D_{Knudsen}	Knudsen diffusion coeffcient $(\mathrm{m}^2/\mathrm{s})$.
$D_{1m,\mathrm{eff}}$	Effective mixture diffusion coefficient for transport in catalyst pores $(\mathrm{m}^2/\mathrm{s})$.
d_p	Diameter of catalyst pellet (m).
$F_{\mathrm{in}_{i,j}}$	Mol flow rate of species i at inlet of cell j (mol/s).
$F_{\mathrm{out}_{i,j}}$	Mol flow rate of species i at outlet of cell j (mol/s).
$\Im$	Radiative heat transfer coefficient.
h^{bed}	Pellet bed heat transfer coefficient $(\mathrm{W}/\mathrm{m}^2 \cdot \mathrm{K})$.
h_i	Enthalpy of species i (J/mol).
ΔH	Enthalpy of reaction (J/mol).
$\vec{j}i$	Diffusive mass flux of species i(kg/m · K).
$\overline{k}_D$	Amphlett decomposition reaction rate constant per unit catalyst mass $(\mathrm{mol}/\mathrm{kg} \cdot \mathrm{s})$ [4].
$\overline{k}_R$	Amphlett reforming reaction rate constant per unit catalyst mass $(\mathrm{m}^3/\mathrm{kg} \cdot \mathrm{s})$ [4].
k''_R	Amphlett reforming reaction rate constant per unit pebble exterior surface area (m/s).
L_{bed}	Characteristic length (m).
M_i	Molecular weight of species i (kg/mol).
m_{cat}	Mass of catalyst (kg).
N_p	Number of pellets.
n	Number of radiation shields.
n_s	Number of species.
p	Pressure (Pa).
Q^{convn}	Heat transferred by convection (W).
q''_{loss}	Heat flux to the surroundings $(\mathrm{W}/\mathrm{m}^2)$.
Q^{rxn}	Heat generated by chemical reaction (W).
Re	Reynolds number.
$\overline{R}$	Universal gas constant $(\mathrm{J}/\mathrm{mol} \cdot \mathrm{K})$.
R_I	Catalyst pellet internal diffusive resistance (s/m).
R_O	Catalyst pellet external convective resistance (s/m).
r_{cat}	Catalyst pore radius (m).
r'''	Volumetric reaction rate $(\mathrm{mol}/\mathrm{m}^3 \cdot \mathrm{s})$.
r''	A real reaction rate $(\mathrm{mol}/\mathrm{m}^2 \cdot \mathrm{s})$.
S_{CR}	Energy source term $(\mathrm{W}/\mathrm{m}^3)$.
$\vec{S_m}$	Momentum source term $(\mathrm{kg}/\mathrm{s}^2 \cdot \mathrm{m}^2)$.
Sc	Schmidt number.

Manuscript received June 22, 2004; revised September 12, 2005. This work was performed under the auspices of the U. S. Department of Energy by the Lawrence Livermore National Laboratory, University of California, under Contract W-7405-Eng-48. Subject Editor O. Tabata.

H. G. Park is with the Department of Mechanical Engineering, University of California at Berkeley, Berkeley, CA 94720 USA. He is also with the Center for Meso, Micro and Nano Technology, Lawrence Livermore National Laboratory, Livermore, CA 94550 USA (e-mail: park15@llnl.gov).

J. A. Malen, R. Greif, and C. P. Grigoropoulos are with the Department of Mechanical Engineering, University of California at Berkeley, Berkeley, CA 94720 USA.

W. T. Piggott, III, J. D. Morse, M. A. Havstad, and R. Upadhye are with the Center for Meso, Micro and Nano Technology, Lawrence Livermore National Laboratory, Livermore, CA 94550 USA.

Digital Object Identifier 10.1109/JMEMS.2006.878888

Sh	Sherwood number.
SMR	Steam to methanol ratio.
T	Temperature (K, °C).
t	Time (s).
$\vec{u}$	Velocity (m/s).
V	Volume (m^3).
w'''_{bed}	Catalyst loading density $(\mathrm{kg/m}^3)$.
x_i	Mole fraction of species i.
$\varepsilon_{\mathrm{bed}}$	Void fraction of catalyst bed.
ε_p/τ_p	Ratio of catalyst pellet void fraction to pore tortuosity.
$\varepsilon_1, \varepsilon_2, \varepsilon_s$	Total hemispherical emissivity of surface 1, 2, or radiation sheild.
Γ	Thermal conductivity (W/m·K).
η_p	Catalyst pellet effectiveness.
Λ	Thiele modulus.
μ	Viscosity $(\mathrm{kg/m \cdot s})$.
ρ	Density $(\mathrm{kg/m}^3)$.
ρ_i	Mass concentration of species i (kg/m^3.
σ	Stefan–Boltzmann constant $(\mathrm{W/m}^2 \cdot \mathrm{T}^4)$.

Subscripts

bed	Pellet bed characteristic.
cat	Catalyst.
D	Decomposition reaction.
i	Species ($1 = \mathrm{CH_3OH}$, $2 = \mathrm{H_2O}$, $3 = \mathrm{CO_2}$, $4 = \mathrm{CO}$, $5 = \mathrm{H_2}$).
j	Axial cell location.
p	Pellet characteristic.
R	Reforming reaction.
W	Water-gas shift reaction.
wall	Channel wall.

I. Introduction

OVER the past two decades, there has been increased research in small fuel cells, along with miniaturized systems for providing them fuel on demand. With the difficulty of storing hydrogen in high concentrations for portable applications, conversion of hydrocarbon fuels to hydrogen-rich gas streams for fuel cells via a catalytic microreactor represents a viable approach to high energy density, microfuel cell system implementation [1]. While several candidate fuels for on-demand generation of hydrogen rich fuel feeds have been investigated [2], [3], methanol steam reforming has been preferred due to the lack of inter carbon bonds in methanol, hence relatively low reforming temperatures (200–300 °C). Other advantages for methanol steam reforming include the limited carbon monoxide production, typically <5000 ppm, and a higher hydrogen fraction in the reformate compared to that of partial oxidation. A MEMS based micro reformer has the advantages of small features, integrated components, and effective thermal coupling of heat source and reactor bed. Because of these advantages, it is reasonable to expect that micro reformers will be developed for the eventual integration of micro fuel cell systems.

Provided these advantages, realization of a microfuel cell system utilizing methanol steam reforming presents a delicate balance from both a thermal and chemical system standpoint. These system balance issues are even more severe when considering the use of low temperature, proton exchange membrane fuel cells that are highly susceptible to CO poisoning of the anode electrode catalyst, and severe dehydration of the electrolyte membrane for temperature excursions $>$ 100°C. As such, prediction of the chemical and thermal properties of a methanol steam reformer provides critical insight into the nominal operating conditions and performance of the microreactor.

According to Amphlett *et al.* [4], methanol experiences two overall reactions in a reformer in the presence of $\mathrm{Cu/ZnO/Al_2O_3}$ catalyst

$$\mathrm{CH_3OH + H_2O \longleftrightarrow CO_2 + 3H_2} \quad (1)$$

$$\mathrm{CH_3OH \longrightarrow CO + 2H_2}. \quad (2)$$

Reaction (1), called reforming, is a primary reaction in the methanol steam reforming process. Some portion of the methanol decomposes to produce carbon monoxide via reaction (2). In the presence of water, the three products adjust their compositions via the water-gas shift reaction

$$\mathrm{CO + H_2O \longleftrightarrow CO_2 + H_2}. \quad (3)$$

For many applications, the reformer working temperature varies from 200 to 300 °C, where the dry product composition is such that the proportions of $\mathrm{H_2/CO_2/CO}$ are approximately 74/24/2 by volume.

One of the essential issues associated with methanol steam reforming for fuel cells is CO contamination. However small, CO always exists in the reformate feed due to reaction (2) and (3), and will poison and ultimately deactivate the Pt catalyzed anode of some fuel cells. Since the poisoning amount of CO is a few tens of ppm, it is important to estimate accurately the small amount of CO produced. Thermal management is also important because of the high surface to volume ratio of the micro reformer and its high operating temperature. Efficient thermal isolation, start-up time, and losses are primary considerations for miniature fuel cells using microreformers for portable applications.

II. Chemical Kinetics

In order to adequately validate the models presented in the following sections, chemical kinetics for steam reforming reactions were applied. The objective is to compare the results of the various models with experimental results in order to develop the models with various levels of computational efficiency necessary for accurate prediction of methanol steam reforming in microreactor devices.

The chemical kinetics of Amphlett *et al.* [4], which neglects the water gas shift reaction, is presented here

$$r'''_{\mathrm{R}} = c_1 C_{\mathrm{Amp}} \overline{k}_{\mathrm{R}} w'''_{\mathrm{bed}}, \quad r'''_{\mathrm{D}} = C_{\mathrm{Amp}} k_{\mathrm{D}} w'''_{\mathrm{bed}} \quad (4)$$

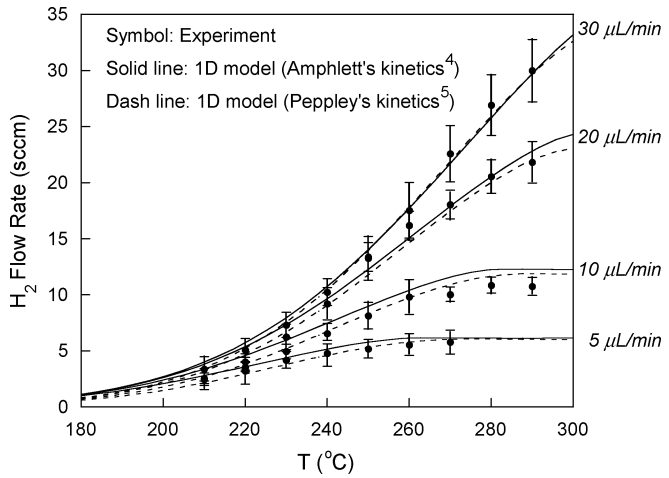

Fig. 1. Comparison of the 1-D flow simulation predictions and the measured H_2 output, as a function of temperature for four input flow rates: 5, 10, 20, 30 μL/min. Error bars represent the 95% confidence interval.

$$\overline{k}_{\mathrm{R}} = (A_{\mathrm{R}} + B_{\mathrm{R}} \ln(\mathrm{SMR})) \exp\left(-\frac{E_{\mathrm{R}}}{\overline{R}T}\right) \tag{5}$$

$$\overline{k}_{\mathrm{D}} = A_{\mathrm{D}} \exp\left(-\frac{E_{\mathrm{D}}}{\overline{R}T}\right). \tag{6}$$

Amphlett found that the water gas shift reaction could be neglected without a substantial loss in accuracy. The molecular generation rate of each species is defined as follows, where the subscripts are $1 = CH_3OH$, $2 = H_2O$, $3 = CO_2$, $4 = CO$, and $5 = H_2$

$$\begin{aligned} r_1''' &= -r_R''' - r_D''' \\ r_2''' &= -r_R''' \\ r_3''' &= r_R''' \\ r_4''' &= r_D''' \\ r_5''' &= 3r_R''' + 2r_D'''. \end{aligned} \tag{7}$$

C_{Amp}, an empirically determined constant in (4), is a modification to Amphlett's original kinetics that accounts for the difference in activity and catalyst effectiveness between his C18HC catalyst and the BASF catalyst used here. Catalyst effectiveness is defined as the ratio of the actual consumption rate of methanol divided by that for a particle with an infinite diffusion coefficient. A value of 2.2 was determined for C_{Amp} by using a least squares fit to the experimental data shown in Fig. 1, which will be discussed in a later section. This value is reasonable because the BASF catalyst is more active than the C18HC catalyst [4], and for our work the catalyst effectiveness is enhanced because smaller particles with shorter diffusion distances were used.

The chemical kinetics of Peppley *et al.* [5] was also used in the one-dimensional (1-D) flow simulation. Peppley's kinetics includes the water-gas shift reaction, and since it is based upon BASF catalyst of similar particle size, we used it without modification.

III. Mass Transport

Mass transport was not considered in the calculation because our test results indicated that the reaction was dominated by the reaction rate, rather than the diffusion rate. The analytical prediction of mass transport that follows confirms this result.

Our analysis is based on the diffusion of methanol from the free stream, to the surface of the catalyst pellet, and into the catalyst pores. Methanol is chosen because it is in lower concentration than water, and hence has a higher diffusive resistance. Two resistances exist between the free stream and catalyst surface; the first is an outer convective resistance (R_O) between the pellet surface and the free stream, and the second is an internal resistance (R_I) within the pellet that accounts for diffusion within its pores and the kinetic rate of the chemical reaction at the catalyst surface [6]. The molar flux of methanol at the pellet surface r_R'' is related to the concentration of methanol in the free stream c_1, the concentration of methanol in the catalyst $c_{1,\mathrm{cat}}$, and the two resistances by

$$r_R'' = \frac{c_1 - c_{1,\mathrm{cat}}}{R_O + R_I} = \frac{c_1}{R_O + R_I}. \tag{8}$$

$c_{1,\mathrm{cat}}$ is eliminated (8) in because the concentration of methanol in the catalyst is zero.

The outer convective resistance is defined as

$$R_O = \frac{1}{G_m} = \frac{L_{\mathrm{char}}}{\mathrm{Sh} D_{1m}} \tag{9}$$

where G_m is the convective mass transfer coefficient defined by the characteristic diffusion length in the pellet bed L_{char}, the Sherwood Number for a pellet bed Sh, and the binary diffusion coefficient of methanol in the mixture, D_{1m}. The internal resistance is defined as

$$R_I = \frac{1}{(V_p a_p / A_p)\eta_p k_R''} \tag{10}$$

where V_p is volume of the pellet, a_p is the total surface area per unit volume of the catalyst pellet, A_p is the external surface area of the pellet (this does not include the internal surface area of the pores), η_p is the catalyst effectiveness, and k_R'' is the first order kinetic rate constant for the reaction. The catalyst effectiveness is the ratio of the actual reaction rate divided by the reaction rate in a pellet with an infinite diffusion rate. The quantity $(V_p a_p / A_p)$ represents the internal surface area of the porous catalyst pellet per unit surface area of the pellet exterior. Amphlett's $\overline{k}_R$ defined per unit catalyst mass, and k_R'' from (10), defined per unit total catayst surface area, are related as follows:

$$k_R'' = \frac{C_{\mathrm{Amp}} \overline{k}_R \rho_{\mathrm{cat}}}{a_p} \tag{11}$$

where ρ_{cat} is the density of the catalyst. To find the rate at which methanol is reformed per unit volume of the reactor bed, r_R''

is multiplied by the area-to-volume ratio $A_{\rm Bed}/V_{\rm Bed}$. For N_p pellets

$$\frac{A_{\rm Bed}}{V_{\rm Bed}} = \frac{N_p A_p}{V_{\rm Bed}} = \left(\frac{N_p V_p}{V_{\rm Bed}}\right)\left(\frac{A_p}{V_p}\right) = (1-\varepsilon_b)\left(\frac{A_p}{V_p}\right). \tag{12}$$

Hence, the volumetric generation rate of methanol is written in terms of the mol flux at the pellet exterior surface as

$$r_R''' = \frac{r_R''(1-\varepsilon_{\rm bed})A_p}{V_p}. \tag{13}$$

By substituting (9)–(13) into (8), we find

$$r_R''' = \left(\frac{(1-\varepsilon_{\rm bed})A_p}{V_p}\right)\frac{c_1}{\frac{L_{\rm char}}{{\rm Sh}D_{1m}} + \frac{1}{(V_p/A_p)\eta_p C_{\rm Amp}\overline{k}_R\rho_{\rm cat}}}. \tag{14}$$

In the special case that the outer convective resistance is much less than the internal resistance ($R_O \ll R_I$), and the catalyst effectiveness is nearly unity ($\eta_p \approx 1$), (14) reduces to (4), where mass transfer was neglected

$$\begin{aligned} r_R''' &= \left(\frac{(1-\varepsilon_{\rm bed})A_p}{V_p}\right) c_1 (V_p/A_p) C_{\rm Amp}\overline{k}_R\rho_{\rm cat} \\ &= c_1(1-\varepsilon_{\rm bed})C_{\rm Amp}\overline{k}_R\rho_{\rm cat} \\ &= c_1 C_{\rm Amp}\overline{k}_{\rm R} w_{\rm bed}'''. \end{aligned} \tag{15}$$

These conditions are met by our pellet bed reactor. Table I poses the equations and representative values for each of the parameters in (14). The operating parameters were chosen at the channel inlet. The calculated values shown in Table I illustrate the R_O is three orders of magnitude less than R_I, and that η_p is very nearly unity.

Equation (14) can also justify the use of $C_{\rm Amp}$. In the case that Amphlett used much larger pellets, his effectiveness was likely smaller than unity. For example, suppose that η_p for Amphlett's catalyst was 0.45, and the condition of $R_O \ll R_I$ is met. Since he neglected η_p, this 0.45 is built into the values of his empirically determined constants, A_R and B_R, from (5). Hence, the unrealistic 0.45 factor that Amphlett associated with the kinetic rate is actually associated with the diffusive resistance inside the catalyst pores. This value was carried forth to our analysis of smaller catalysts, where the diffusive resistance is negligible ($\eta_p \approx 1$). As a result, its prediction was a factor of $1/0.45 = 2.2$ different than we'd expect. So the addition of $C_{\rm Amp}$ offsets the difference in the effectiveness of Amphlett's and our catalyst pellets.

TABLE I
MICROREFORMER PROPERTIES AT INLET FOR 5 μL/min FLOW RATE

Parameter	*Definition or Reference*	*Value*
d_p (m)	*measurement*	280E-6
V_p (m^3)	$\pi d_p^3/6$	1.15E-11
A_p (m^2)	πd_p^2	2.46E-7
ε_{bed}	*measurement*	0.5
r_{cat} (m)	*Catalyst pore size*	1.0E-7
m_{cat} (kg)	*measurement*	38.5E-6
V_{bed} (m^3)	*measurement*	5.0E-8
ε_p/τ_p	*Mills*[6]	0.2
a_p (m^{-1})	*Peppley*[5]	1.92E8
ρ_{cat} (kg/m^3)	$m_{cat}/V_{bed}(1-\varepsilon_v)$	1920
c_1 (mol/m^3)	*measurement*	12.26
T (^{o}C)	*measurement*	200
Re	*Equation* (29)	5.15
Sc	*Schmidt Number*	0.55
L_{char} (m)	$d_p\varepsilon_v/(1-\varepsilon_v)$	280E-6
Sh	$\left(0.5\,{\rm Re}^{0.5}+0.2\,{\rm Re}^{2/3}\right)Sc^{1/3}$ *for pellet bed*[6]	3.88
D_{1i} (m^2/s)	$1.86\times10^{-7}\frac{\sqrt{T^3\left(1/M_1+1/M_i\right)}}{\sigma_{1i}^2\Omega_D P}$ P [atm], M [g/mol]	per species i
σ_{1i}	*Lennard Jones Parameter (Mills*[6] *A.26)*	per species i
Ω_D	*Lennard Jones Parameter (Mills*[6] *A.28)*	per species i
D_{1m} (m^2/s)	$\frac{(1-x_1)}{\sum_{i=2}^{5}(x_i/D_{1i})}$	4.65E-5
$D_{Knudsen}$ (m^2/s)	$\left(\frac{2}{3}\right)r_{cat}\left(\frac{8\overline{R}T}{\pi M_1}\right)^{1/2}$ *only relevant in catalyst pores*	3.73E-5
D_{1eff} (m^2/s)	$\frac{\varepsilon_p}{\tau_p}\left(\frac{1}{D_{1m}}+\frac{1}{D_{Knudsen}}\right)^{-1}$ *only relevant in catalyst pores*	2.07E-5
$\overline{k}_R$ (m^3/kg·s)	*Equation (5)*	6.43E-4
C_{Amp}	*Empirically determined*	2.2
Λ	$\frac{V_p}{S_p}\left(\frac{k''a_p}{D_{1eff}}\right)^{1/2}$	0.038
η_p	$\frac{1}{\Lambda}\left(\frac{1}{\tanh 3\Lambda}-\frac{1}{3\Lambda}\right)$ *for spherical pellets*	0.9991
R_O(s/m)	*Equation* (9)	4.25
R_I (s/m)	*Equation* (10)	7.89E3

IV. GOVERNING EQUATIONS

The governing equations for mass, momentum, heat, and species conservation are described in this section. Three models were created to predict the hydrogen output of the microreactor, each differing in complexity and computational expense.

Computational fluid dynamics (CFD) was used to model three-dimensional (3-D) mass, momentum, heat transfer in a microreformer. A commercial code (Fluent [7]) was employed to carry out this analysis. TOPAZ3D [10] was used to implement a quasi-3-D simulation that reduced computing time

relative to the 3-D model. This quasi-3-D approach simulated the reacting flow with a 1-D plug flow reactor (PFR), coupled to 3-D heat transfer in the silicon wafer. Finally, we created a fully 1-D model of the microreformer to further reduce computational expense. Like the quasi-3-D model, the 1-D model simulated the reacting flow as a PFR. However, the 1-D model was further simplified by assuming a uniform temperature in the silicon wafer.

A. Conservation Equations and Assumptions of the 3-D Model

The conservation equations for a steady-state reacting flow inside a porous catalyst bed are as follows:

mass conservation:

$$\nabla \cdot (\rho \vec{u}) = 0; \tag{16}$$

momentum conservation:

$$\nabla \cdot (\rho \vec{u}\vec{u}) = \nabla \cdot \mu \nabla \vec{u} - \nabla p + \vec{S}_m(\vec{u}); \tag{17}$$

energy conservation:

$$\nabla \cdot (\rho \vec{u} c_p T) = \nabla \cdot \Gamma \nabla T + S_{\mathrm{CR}} \tag{18}$$

species conservation:

$$\nabla \cdot (\rho_i \vec{u} + \vec{j_i}) = r_i'''/M_i. \tag{19}$$

Equations (16)–(19) were used for the 3-D model. The Ergun equation [12], for porous media was employed to represent the momentum source term in (17)

$$\vec{S}_m(\vec{u}) = -150 \frac{(1-\varepsilon_{\mathrm{bed}})^2}{\varepsilon_{\mathrm{bed}}^3} \frac{\mu}{d_p^2} \vec{u} \tag{20}$$

The thermal conductivity, Γ, in (18) is a volume weighted average of the catalyst bed material $(\mathrm{Cu/ZnO/Al_2O_3})$ and the gas mixture

$$\Gamma = \varepsilon_{\mathrm{bed}} \Gamma_f + (1 - \varepsilon_{\mathrm{bed}}) \Gamma_{\mathrm{s}} \tag{21}$$

Endothermic reactions in the reformer result in an energy source term in (18) that can be represented as

$$\mathrm{S_{CR}} = -\Delta H_{\mathrm{R}} r_{\mathrm{R}}''' - \Delta H_{\mathrm{D}} r_{\mathrm{D}}''' \tag{22}$$

The reactor wall is regarded as no-slip and impermeable. The thermal boundary condition at the wall is based on the thermal resistance concept considering thermal conduction through solid and natural convection to the surroundings at a room temperature. The inlet flow rate, temperature, and SMR are prescribed as boundary conditions. Finally, a zero gauge pressure boundary condition was applied at the outlet.

B. Assumptions of the Quasi-3-D and 1-D Models

The PFR model used for the quasi-3-D and 1-D models is presented here. In the axial (flow) direction the 1-D species conservation equation is

$$\frac{dF_i}{dx} = r_i''' A_c \tag{23}$$

where F_i is the molar flow rate of species i, and A_c is the channel cross sectional area. The forward differencing scheme was used to discretize (23) for numerical solution.

$$\sum_{i=1}^{ns} F_{\mathrm{out}_{i,j}} = \sum_{i=1}^{ns} F_{in_{i,j}} + r_{i,j}''' A_c \Delta x_j \tag{24}$$

$F_{i,j}$ is the molar flow rate of species i in the jth cell (which has length Δx_j). Solution of the PFR system gives entrance and exit molar flow rates for each cell in the flow channel. The momentum conservation equation is unnecessary for the PFR simulation because the model does not intend to resolve the pressure distribution in the channel. The steady flow heat balance on each cell is:

$$\sum_{i=1}^{ns} F_{\mathrm{out}_{i,j}} h_{\mathrm{out}_{i,j}} = \sum_{i=1}^{ns} F_{in_{i,j}} h_{in_{i,j}} + Q_j^{rxn} + Q_j^{\mathrm{convn}} \tag{25}$$

The summation terms give the enthalpy carried into and out of each PFR cell by each species. The heat produced or removed by the progress of the chemical reaction in the system is determined by the solution to the PFR species equations and the heats of reaction. Q_j^{rxn} is defined as

$$Q_j^{rxn} = S_{\mathrm{CR}} A_c \Delta x_j \tag{26}$$

where $\mathrm{S_{CR}}$ is from (22). The convection term defines the coupling between the fluid flow channel and the surrounding solid material (Si wafer). Here we use a convection correlation developed for packed beds [13]:

$$Q_j^{\mathrm{convn}} = h_j^{\mathrm{bed}} A_j^{\mathrm{wall}} \left(T_j^{\mathrm{wall}} - T_j\right) \tag{27}$$

$$h_j^{\mathrm{bed}} = C_1 \mathrm{Re}_j^{C_2} \frac{\Gamma}{d_p} \tag{28}$$

Reynolds number is based on particle diameter and the local fluid properties and velocity in the jth PFR cell.

$$\mathrm{Re} = \left(\frac{\rho u}{\mu}\right)_j d_p \tag{29}$$

The wall temperature T_j^{wall} is variable for the quasi-3-D simulation and depends on the 3-D temperature distribution within the silicon wafer. The facets bounding PFR cell j are used to compute the wall temperature T_j^{wall} and wall area, A_j^{wall}, for convective heat transfer. The wall temperature is assumed constant

and prescribed for the 1-D model. The inlet flow rate, temperature, and SMR are prescribed as boundary conditions for those models.

C. Heat Loss to the Surroundings

The flow relations were coupled to a 3-D finite element conduction model of the silicon wafer by heat flux through the channel wall. Heat loss from the silicon wafer to the surroundings has been modeled with a free convection heat transfer coefficient, h_{fc}

$$q''_{\text{loss}} = h_{fc}(T - T_\infty). \tag{30}$$

Two forms of insulation were considered to reduce heat loss: conventional low conductivity solid insulation and vacuum packaging. The vacuum packaging is modeled using a radiation transport coefficient $\Im$

$$q''_{\text{loss}} = \Im\sigma\left(T^4 - T_\infty^4\right) \tag{31}$$

$\Im$ is determined by material emittances, package geometry, and shield number. For n radiation shields $\Im$ is defined as [14]

$$\Im = \frac{1}{\left(\frac{1-\varepsilon_1}{\varepsilon_1} + \frac{1-\varepsilon_2}{\varepsilon_2} + 1\right) + n\left[2\left(\frac{1-\varepsilon_s}{\varepsilon_s}\right) + 1\right]} \tag{32}$$

where the heat is assumed to be transferred between surfaces of equal area. The bracketed quantity in the denominator represents the insulating value of a single radiation shield.

D. Constituative Laws

Properties such as density, molecular viscosity, and thermal conductivity were calculated assuming an ideal gas mixture. Thus the density was calculated from

$$\rho = \frac{p}{\overline{R}T}M = \frac{p}{\overline{R}T}\sum_i x_i M_i \tag{33}$$

Wilke's formula [6] was employed to calculate the molecular viscosity and thermal conductivity of an ideal gas mixture.

V. Microreactor Design and Fabrication

The microreformer design considered here is a single, serpentine shape microchannel, 1 mm wide, in a $254\ \text{mm} \times 254\ \text{mm} \times 0.5\ \text{mm}$ silicon substrate (Fig. 2). The fabrication sequence is illustrated in Fig. 3. The substrate used is a double side polished, $20\ \Omega - \text{cm}$, boron-doped, 100 mm diameter, $\langle 100\rangle$ silicon wafer with 500 μm nominal thickness. A 1000 Å layer of silicon nitride is deposited by chemical vapor deposition. Resistive heaters are formed by spinning a 1 μm layer of positive photoresist, which is subsequently exposed and developed creating the resistive heater pattern on the front side of silicon substrate. This is followed by sputter deposition of 2000 Å Pt.

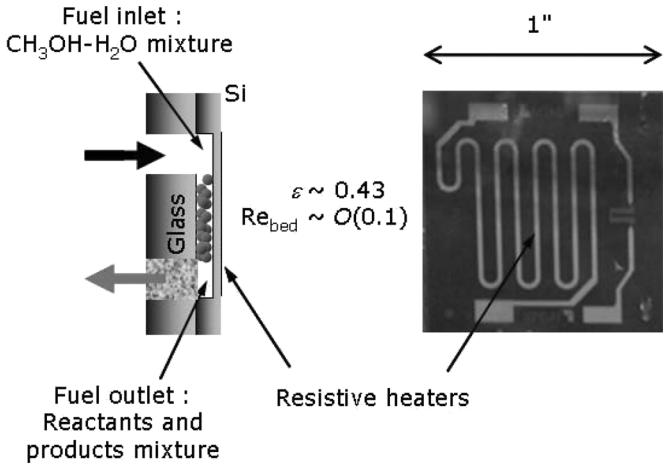

Fig. 2. Cross sectional schematic (left) and top view (right) of catalytic microreactor fabricated in silicon.

Sputter deposition was used for improved adhesion to the silicon nitride without the need for a stick layer. The deposition rate of the Pt was lowered in order to avoid hardening of the photoresist. The photoresist was subsequently removed by soaking in acetone, leaving the resistor pattern as illustrated in Fig. 2. The backside of the wafer was coated with approximately 8.0 μm of photoresist in preparation for deep reactive ion etch of the microchannel structure. The resist is then exposed and developed, after which the exposed silicon nitride is removed from the bottom of the resist pattern using a parallel plate reactive ion etch with a CF_4/O_2 (80:20) gas mixture. Microchannels were etched to an approximate depth of 400 μm using the Bosch process, resulting in reasonably smooth, vertical sidewalls. The wafer was prepared for anodic bonding by first stripping the photoresist, then removing the silicon nitride from the backside of the wafer using a reactive ion etch in the same parallel plate reactor with CF_4/O_2 (80:20) gas mixture. Care was taken to not overetch the nitride as any surface damage may degrade or prevent a good wafer bond. The silicon surface was further prepared by conducting a standard RCA type clean step. The microchannels were sealed by anodically bonding a borosilicate glass wafer to the bare silicon. The glass substrate is 500 μm thick and has 1 mm diameter inlet and outlet vias pre-etched by ultrasonic etching. The wafers were carefully aligned, then bonded at a temperature of 450°C for 1 hour. A slow temperature ramping was used during the anodic bond step in order to avoid effects of thermal stresses on the glass to silicon interface, which can result in cracking or disbonding. The wafer was subsequently diced up using a diamond saw, resulting in the micro reformer device as shown in Fig. 2.

The channel is 125 mm in length. The initial 25 mm are empty and used to superheat the incoming reactants. Reforming takes place in the final 100 mm of the channel, which was filled with 38.5 mg of $Cu/ZnO/Al_2O_3$ catalyst pellets. The catalyst pellets were filtered between 212 μm and 351 μm sieves, then carefully pored into the inlet of the microreactor channel. Porous glass wool was press fit into the microreactor outlet to prevent

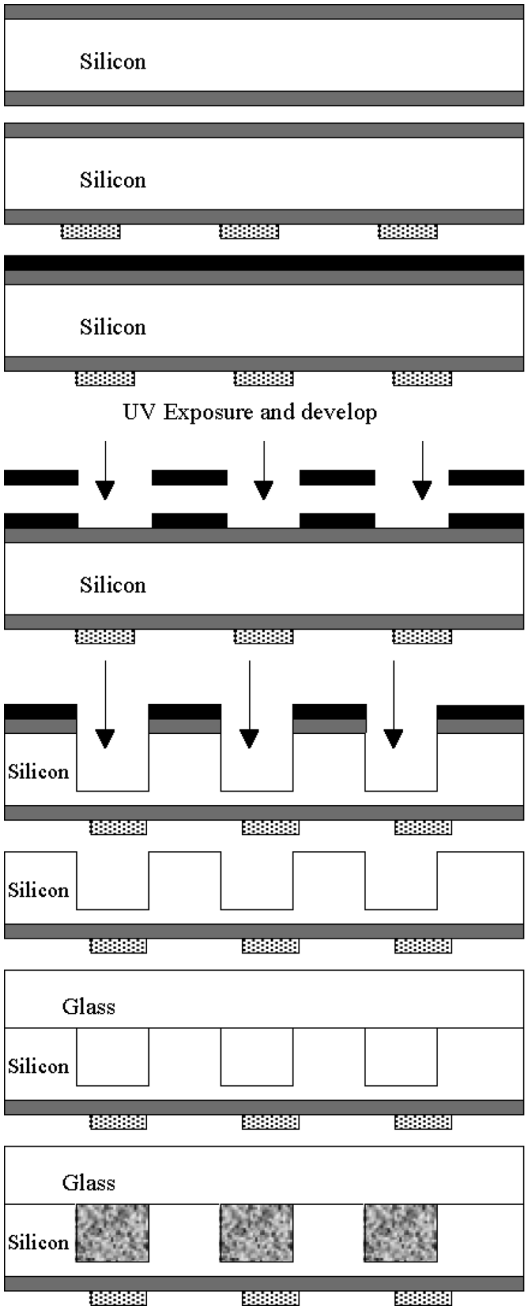

Fig. 3. Fabrication process flow for microfluidic fuel processor; a.) deposit 2000 A CVD nitride on silicon wafer, b.) liftoff patterning of Ti/Pt (200 A/2000 A) resistive heaters, c.) coat thick photoresist for DRIE, d.) expose and develop thick photoresist, e.) reactive ion etch nitride, DRIE silicon microchannels, f.) strip resist and nitride from topside of wafer, g.) anodic bond glass wafer to silicon, h.) fill microchannels with catalyst particles.

catalyst particles from flowing out of the channel. The Pt heaters supply the required amount of heat into the substrate to keep the channel at the desired temperature.

VI. Experimental

The experimental approach is illustrated in Fig. 4. The liquid methanol-water mixture enters the superheater region of the microreactor at room temperature, where it is heated to the temperature of the substrate. The superheated reactants then enter the packed-bed catalytic reforming zone where hydrogen, carbon dioxide and carbon monoxide are formed. At the inlet to the catalyst bed the SMR is 1.1. The reactor temperature was varied between 210 °C and 290 °C for the experiments. Inlet flow rates of liquid reactants were 5, 10, 20, and 30 $\mu\mathrm{L/min}$.

The microreactor chip was placed in an aluminum test fixture that enabled both electrical connections for thermal control, thermocouples, and fluidic connections for the inlet and oulet of the microreactor. External fluidic connections were established using compression fittings on 0.0625″ stainless steel tubing with high temperature O-ring seals. A methanol-water (1:1.1) solution was delivered to the microreactor with a syringe pump. Flow rates varied from 5–30 $\mu\mathrm{L/min}$. The pressure drop across the microreactor was monitored with a pressure gauge at the inlet as shown. Microreactor temperature was monitored using a thermocouple attached to the surface of the silicon chip. The experiment monitored both the conversion of the methanol-water mixture and the concentration of carbon monoxide in the outlet flow stream. Conversion was determined by measuring the output flow rate of total reaction byproducts. In order to accurately measure the outlet flow, a condenser was placed at the outlet to remove any unreacted water or methanol from the flow stream, then a flow meter measured the remaining flow. Total outlet flow was averaged over a 15-min period for each experimental point. Once each experimental condition stabilized for each data point, the outlet flow was redirected through a three-way valve to a nondispersive infrared spectrometer (NDIR). The NDIR provided an accurate measurement of the total carbon monoxide in the outlet flow stream.

VII. Results

The experimentally measured outlet hydrogen flow rate from the silicon steam reformer is shown in Fig. 1 for a range of inlet flow rates over a broad temperature range. Fig. 1 further compares the experimental measurements with two sets of curves calculated with the 1-D flow simulation. The solid lines represent the modified Amphlett [4] kinetics, and the dotted lines represent the Peppley [5] kinetics. While both kinetic models agree adequately with the data, and are acceptable for our design work, the modified Amphlett [4] kinetics more closely match the experimental data at higher temperatures, and thereby provide a more versatile design model.

Results for the experimentally measured conversion efficiency are compared to the 3-D, quasi-3-D, and 1-D model in Fig. 5 for inlet flow of 10 $\mu\mathrm{L/min}$ at various temperatures. In the 1-D model for this example, the modified Amphlett [4] kinetics was used. This comparison illustrates that all three models show good agreement with experiment. Hence, as long as the assumptions and boundary conditions are valid, the 1-D model is a computationally efficient and accurate design tool. The 3-D or quasi-3-D models, however, may be utilized to validate the thermal uniformity and boundary conditions assumptions for the 1-D case at select temperatures. In addition, they may be applied to reacting flow designs that uses complex geometry. Fig. 6 additionally compares the experimentally measured carbon monoxide concentration in the outlet flow stream with the 3-D, quasi-3-D, and 1-D models for inlet flow of 10 $\mu\mathrm{L/min}$. Again, all three models show favorable comparison to experiment over a broad operating temperature range

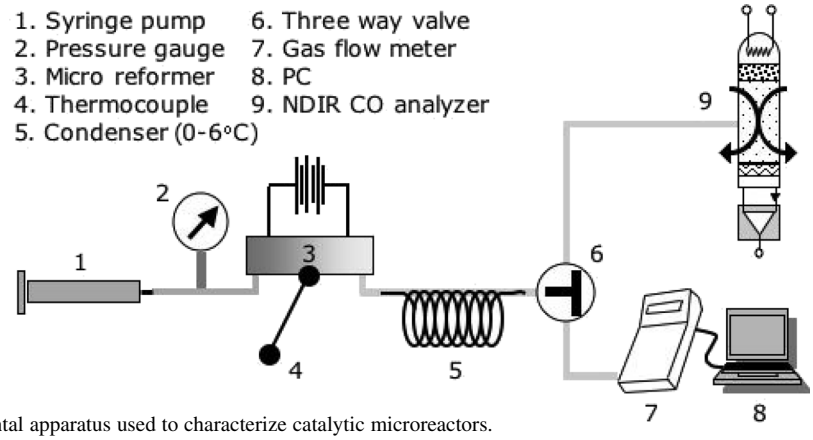

Fig. 4. Schematic of experimental apparatus used to characterize catalytic microreactors.

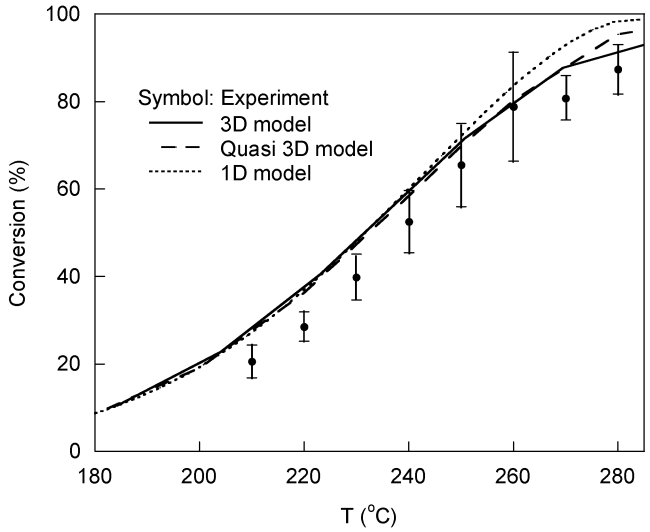

Fig. 5. Comparison of modeled and experimentally measured steam reforming conversion versus temperature for a catalytic microreactor at 10 $\mu\mathrm{L/min}$ inlet liquid flow rate.

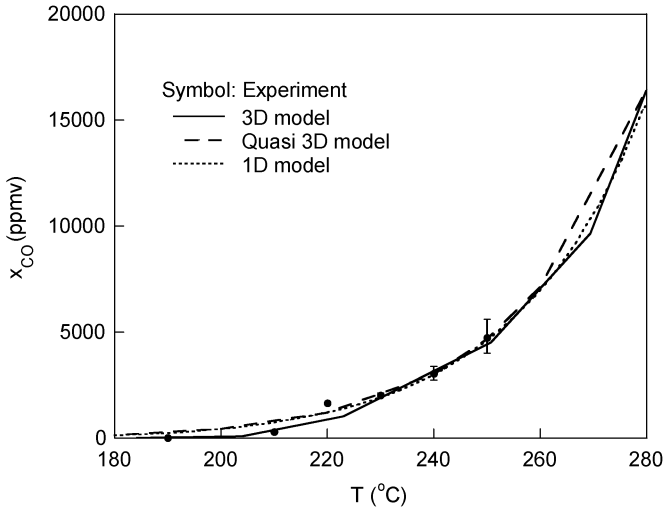

Fig. 6. Comparison of experimentally measured and modeled carbon monoxide content versus temperature in the outlet flow of the steam reforming catalytic microreactor with 10 $\mu\mathrm{L/min}$ inlet liquid flow rate.

for the silicon steam reforming microreactor. The ability of the 1-D flow simulation model to provide accurate assessment of reaction byproducts further illustrates the robustness and versatility of this approach.

Thermal insulation aspects for the silicon steam reforming microreactor were evaluated. Two forms of thermal isolation are considered here. Low-thermal conductivity solid insulations are perhaps the simplest option but only for the most exotic and difficult to handle materials (low conductivity evacuated aerogels) is performance approaching adequate. Highly reflective radiative shields separated by thin evacuated gaps are potentially superior but more complex, expensive and difficult to implement. These two options were compared (Fig. 7). Using simple 1-D heat transfer relations [see (30)–(32)] for the design at hand, i.e., a one-inch square chip operating at 250 °C which is producing a reformate fuel feed for a 2 to 3 W fuel cell. Steady-state heat loss from the two sides of such a wafer should be 0.2 to 0.3 W or less to maintain adequate system efficiency. Further, applications of microfuel cell systems often require an exterior temperature of less than 40 °C to limit thermal signature and heat loss. Both the 3 and 4 shield cases in Fig. 7 satisfy the low-temperature and low-heat loss criteria but the graph presents idealized results in the sense that shield gap is infinitesimal and conductive transport is zero. In practice increased heat loss will result from conduction and real gap sizes. The effect of these two mechanisms is to move up and to the left from the radiative curve shown toward the conduction curve.

Fig. 8 shows the steady-state thermal profile of the exterior of the silicon wafer for a radiatively shielded $(\mathrm{F} = 0.05)$ case. Temperatures are elevated on the surface of the microchannel despite the endothermic heat of reaction because the $\mathrm{I^2R}$ heating is applied over the microchannel on the backside of the channel (as seen in Fig. 2). Thermal gradients are small $(< 10\,^{\circ}\mathrm{C})$ due to the high-thermal conductivity of Si (148 $\mathrm{W/m \cdot K}$). A constant wall temperature approximation, as assumed by the 1-D flow simulation model, is adequate based on small thermal gradients.

Insulating with polyimide foam or evacuated silicon powder is viable in that these materials are available but exterior surface temperatures are too high (172°C for Kapton and 83°C for Si powder) given the practical thicknesses we have posed. Comparison of the radiatively insulated options shows that reducing the radiative transport by adding shields or decreasing shield emissivity is beneficial. Cheap and simple means of obtaining low emissivity and negligible conduction are being sought.

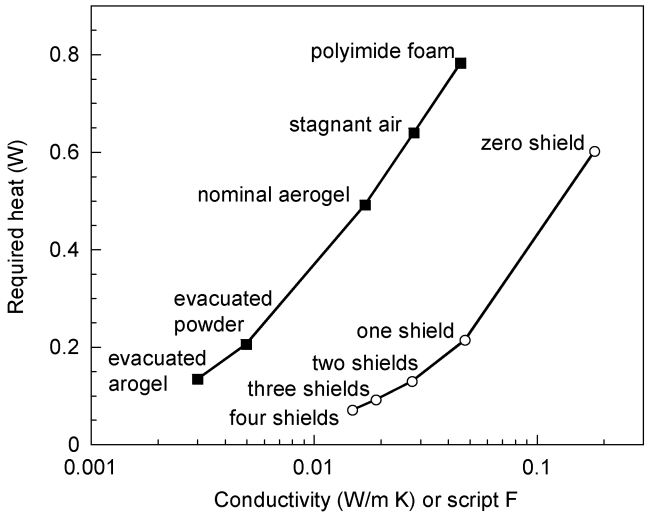

Fig. 7. Comparison of conductive and radiative insulation options. See (32) for definition of script F.

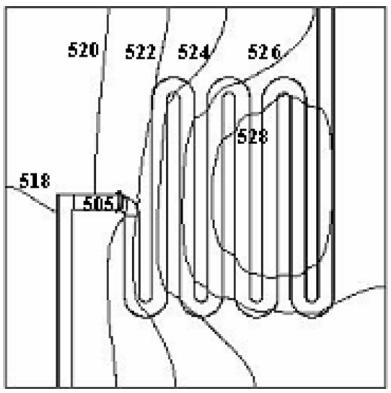

Fig. 8. Temperature profile (K) of the microreactor surface during a steady-state operation; average temperature is 512 K and temperature difference is within 10 K across 2 cm, except for the small inlet region.

VIII. Conclusion

A micro methanol steam reforming device fabricated in silicon has been described. Full 3-D, quasi-3-D, and 1-D models were described and compared to the experimental performance of the microreactor over a range of operating temperatures and reactant flow conditions. Comparison of models with experimental results shows good agreement over a range of operating conditions. We found that Amphlett's kinetics for methanol reforming provided accurate results, and that for our operating conditions the reforming reaction could be modeled without mass transport considerations. The 1-D model provided a rapid analytical tool to assess the performance of the microreactor, and subsequent prediction of performance over a range of flows and temperatures. Further evaluation of thermal insulation and heat loss for the steam reforming device provide a packaging approach for efficient system integration.

References

[1] J. D. Morse, A. F. Jankowski, R. T. Graff, and J. P. Hayes, "Novel proton exchange membrane thin-film fuel cell for microscale energy conversion," *J. Vac. Sci. Technol. A*, vol. 18, no. 4, pp. 2003–2005, 2000.

[2] L. F. Brown, "A comparative study of fuels for on-board hydrogen production for fuel-cell-powered automobiles," *Int. J. Hydrogen Energy*, vol. 26, no. 4, pp. 381–397, Apr. 2001.

[3] F. Joensen and J. R. Rostrup-Nielsen, "Conversion of hydrocarbons and alcohols for fuel cells," *J. Power Sources*, vol. 105, no. 2, pp. 195–201, Mar. 2002.

[4] J. C. Amphlett, K. A. M. Creber, J. M. Davis, R. F. Mann, B. A. Peppley, and D. M. Stokes, "Hydrogen production by steam reforming of methanol for polymer electrolyte fuel cells," *Int. J. Hydrogen Energy*, vol. 19, no. 2, pp. 131–137, Feb. 1994.

[5] B. A. Peppley, J. C. Amphlett, L. M. Kearns, and R. F. Mann, "Methanol-steam reforming on $Cu/ZnO/Al_2O_3$ catalysts. Part 2. A comprehensive kinetic model," *Appl. Catalysis A*, vol. 179, no. 1, pp. 31–49, Apr. 1999.

[6] A. F. Mills, *Mass Transfer*. Englewood Cliffs, NJ: Prentice-Hall, 2001.

[7] *"Fluent User Guide v6,"* Fluent Inc., 2001.

[8] H. G. Park, J. Chung, C. P. Grigoropoulos, R. Greif, M. Havstad, and J. D. Morse, "A methanol steam reforming microreactor for proton exchange membrane micro fuel cell system," in *Proc. Hydrogen and Fuel Cells 2003 Conf. Trade Show*, Vancouver, B.C., Canada, Jun. 12–14, 2003.

[9] H. G. Park, W. T. Piggott, J. Chung, J. D. Morse, M. Havstad, C. P. Grigoropoulos, R. Greif, W. Benett, D. Sopchak, and R. Upadhye, "Transport in a microfluidic catalytic reactor," in *Proc. 2003 Summer Heat Transfer Conf.*, Las Vegas, NV, Jul. 21–23, .

[10] A. B. Shapiro, TOPAZ3D-A Three Dimensional Finite Element Heat Transfer Code Univ. Calif., Lawrence Livermore Nat. Lab., Rep. UCID-20484, 1985.

[11] M. Havstad, "Surface chemistry effects in finite element modeling of heat transfer in micro fuel cells," in *MSM 2001*, Mar. 2001.

[12] S. Ergun, "Fluid flow through packed columns," *Chem. Eng. Progress*, vol. 48, pp. 89–94, 1952.

[13] D. Azbel, *Fundamentals of Heat Transfer for Process Engineering*. New York: Noyes, 1984.

[14] A. F. Mills, *Heat Transfer*. Englewood Cliffs, NJ: Prentice-Hall, 1999.

Hyung Gyu Park received the B.S. and M.S. degrees in mechanical engineering from Seoul National University, Seoul, Korea, in 1992 and 2000, respectively.

He has been a graduate student with the Department of Mechanical Engineering, University of California, Berkeley, since 2001, where he is pursuing the Ph.D. degree. In 2000, he joined the Seoul National University Institute of Advanced Machinery and Design as an Assistant Researcher. Since 2002, he has been supported by and worked concurrently in the Student Employee Graduate Research Fellowship (SEGRF) program of the Lawrence Livermore National Laboratory (LLNL). His research interests encompass heat transfer system design assisted by computational fluid dynamics (CFD) and experiment, microelectrocmechanical systems (MEMS), microchemical systems related to catalytic microreactors and fuel cells, and micronanofluidics combining microfabrication and nanotechnology. His current research projects include carbon nanotube-based nanofluidics and related physics, as well as interactions between quantum dot fluorescence and laser light.

Jonathan A. Malen received the B.S. degree in mechanical engineering from the University of Michigan, Ann Arbor, in 2000 and the M.S. degree in nuclear engineering from the Massachusetts Institute of Technology (MIT), Cambridge, in 2003.

Following his undergraduate degree, he entered the Professional Development Program at the Defense Nuclear Facilities Safety Board, which funded the M.S. Degree and a one year internship at the Center for Meso, Micro, and Nano Technology at Lawrence Livermore National Laboratory. He is currently a Ph.D. degree candidate in the Mechanical Engineering Department, University of California, Berkeley.

Mr. Malen is a National Defense Science and Engineering Graduate Fellow, and a member of Tau Beta Pi, ASME, and ANS.

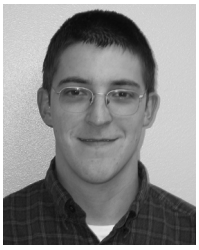

W. Thomas Piggott, III received the B.S. and M.S. degrees, both in mechanical engineering, in 2000 and 2001, respectively, from the University of Illinois at Urbana-Champaign.

He has been with the New Technologies Engineering Division (NTED), Lawrence Livermore National Laboratory, as a mechanical engineer and analyst since 2002. His areas of interest include a broad interest in thermal and fluid sciences including multiphase flow, reacting materials, energy systems, and computational modeling. Current work includes combustion, heat transfer, and accelerator design.

Jeffrey D. Morse received the B.S. and M.S. degrees in electrical engineering from the University of Massachusetts in 1983 and 1985, respectively. He received the Ph.D. degree in electrical engineering from Stanford University, Stanford, CA, in 1992, completed concurrently with his research activities at Lawrence Livermore National Laboratory (LLNL).

He has been a member of the scientific staff of the Center for Meso, Micro and Nano Technology (CMMNT), LLNL, since 1985. His research interests and technical project areas include field emission displays, microelectromechanical systems (MEMS) and microfluidic devices, sensors, and systems. Current areas of research include microchemical systems, catalytic microreactors, fuel cells, and microfluidic devices and technologies.

Ralph Greif received the B.M.E. degree from New York University, New York. He received the M.S. degree from the University of California at Los Angeles and the M.A. and Ph.D. degrees from Harvard University, Cambridge, MA.

He was a Postdoctoral Research Fellow at Harvard University and subsequently joined the faculty of the University of California at Berkeley. Prior industrial experience includes engineering positions with the Hughes Research and Development Laboratories and the Raytheon Research Laboratories. He is currently a Professor with the Department of Mechanical Engineering, University of California at Berkeley. His research interests include heat and mass transfer and fluid mechanics, microscale transport and cooling, fuel cells, laser material interactions, materials processing and deposition, turbulent transport, natural convection, two phase flows, and thermosyphons.

Costas P. Grigoropoulos received the Diploma degrees in naval architecture and marine engineering in 1978, and in mechanical engineering in 1980, from the National Technical University of Athens, Greece. He received the M.Sc. degree in 1983, and the Ph.D. degree in 1986, both in mechanical engineering from Columbia University, New York.

He is a Professor with the Department of Mechanical Engineering, University of California at Berkeley. His research interests (www.me.berkeley.edu/ltl/ltl.html) are in laser materials processing and micromachining, radiative and thermal properties of thin-film materials, laser-induced thin film crystal growth for TFTs, fabrication of flexible electronics, hydrogen storage, advanced energy applications, and ulrafast laser interactions with materials. A variety of experimental techniques are utilized for probing microscopic transport phenomena and testing miniature devices, including femtosecond time-resolved imaging and spectroscopy, noncontact fast temperature measurement via multicolor pyrometry, microparticle imaging velocimetry (μPIV), infrared thermal velocimetry, laser-induced fluorescence, absorption imaging, mass spectroscopy, emission spectroscopy, interferometry, and high-speed visualization. Research is being carried on nanoscale surface modification and probing of nanoscale chemical analysis and transport using near-field scanning optical microscopy (NSOM) in both apertureless and fiber coupled modes.

Dr. Grigoropoulos is a Fellow of the American Society of Mechanical Engineers (ASME) and an Associate Editor for the *Journal of Heat Transfer* and the *International Journal of Heat and Mass Transfer*.

Mark A. Havstad received the B.S. degree from Yale University, New Haven, CT, the M.S. degree from Colorado State University, and the Ph.D. degree from Stanford University, Stanford, CA.

He is an engineer with the New Technologies Engineering Division, Lawrence Livermore National Laboratory. He works in finite-element heat transfer, optical and radiative properties, thermal effects on reentry, and aging of sealed assemblies.

Ravi Upadhye received the B.Tech. and M.S. degrees in chemical engineering from the Indian Institute of Technology, Bombay and the University of New Brunswick, respectively. He received the Ph.D. degree in chemical engineering from the University of California at Berkeley, in 1974.

He has been with Lawrence Livermore National Laboratory (LLNL) since 1984. Currently he is the Materials Program Leader (acting) for Energy and Environment in Chemistry and Materials Science Directorate. He worked in a number of capacities at Air Products and Chemicals, Allentown, PA, prior to joining LLNL. His expertise is in process design, simulation and optimization, and in chemical reaction engineering. He has more than 50 publications and holds four patents.

Dr. Upadhye is a Fellow of the American Institute of Chemical Engineers.